Supplemental material

Singhal et al., **https://doi.org/10.1084/jem.20180008**

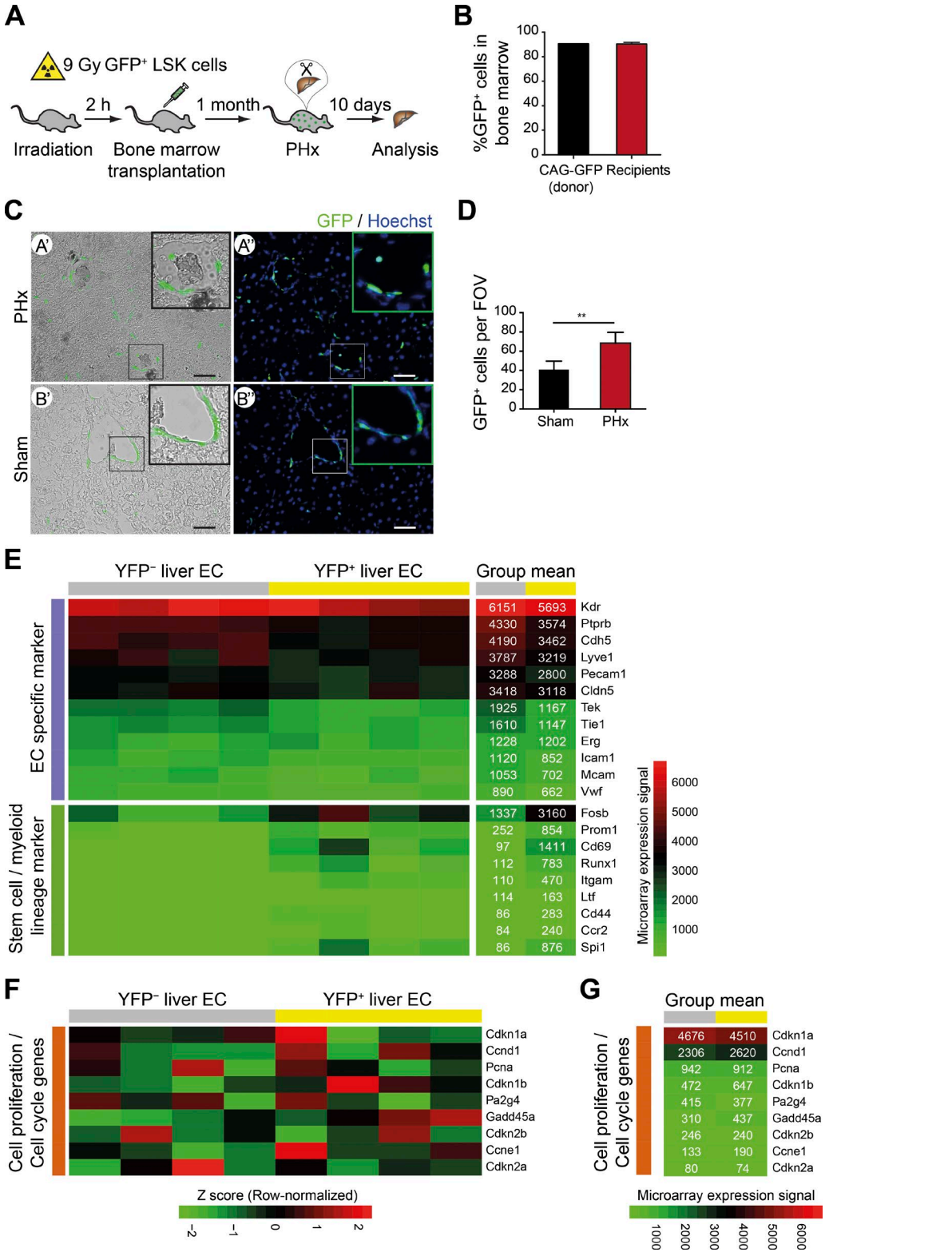

Figure S1. **Irradiation-conditioned bone marrow chimeras illustrate recruitment of BMDMCs in the regenerating liver. (A)** Experimental outline of PHx-induced liver regeneration in irradiation-conditioned GFP+ bone marrow–transplanted mice. **(B)** Whole bone marrow cells were isolated from the CAG-GFP donor mice as well as the recipient mice and were analyzed by FACS to evaluate the donor chimerism (mean ± SD, $n_{CAG\text{-}GFP}$ = 1, $n_{Recipient}$ = 6 mice). **(C)** Microscopic analysis of liver sections from sham-operated (lower panels, B′ and B″) and PHx mice (upper panels, A′ and A″) shows bone marrow–derived GFP+ cells integrated into the liver vasculature. Scale bars, 50 µm. **(D)** The plot shows the GFP+ cell count per field of view (FOV) in the sham-operated and PHx mice (mean ± SD, n = 6 mice). **, P < 0.01 (two-tailed Student's t test). **(E)** Microarray-based gene expression analysis of YFP− resident liver ECs and YFP+ bone marrow–derived liver ECs was performed. Group mean heat map shows the average of biological replicates (n = 4 mice). **(F)** The heat map represents expression of cell cycle regulatory genes. **(G)** Group mean heat map shows the average of biological replicates (n = 4 mice).

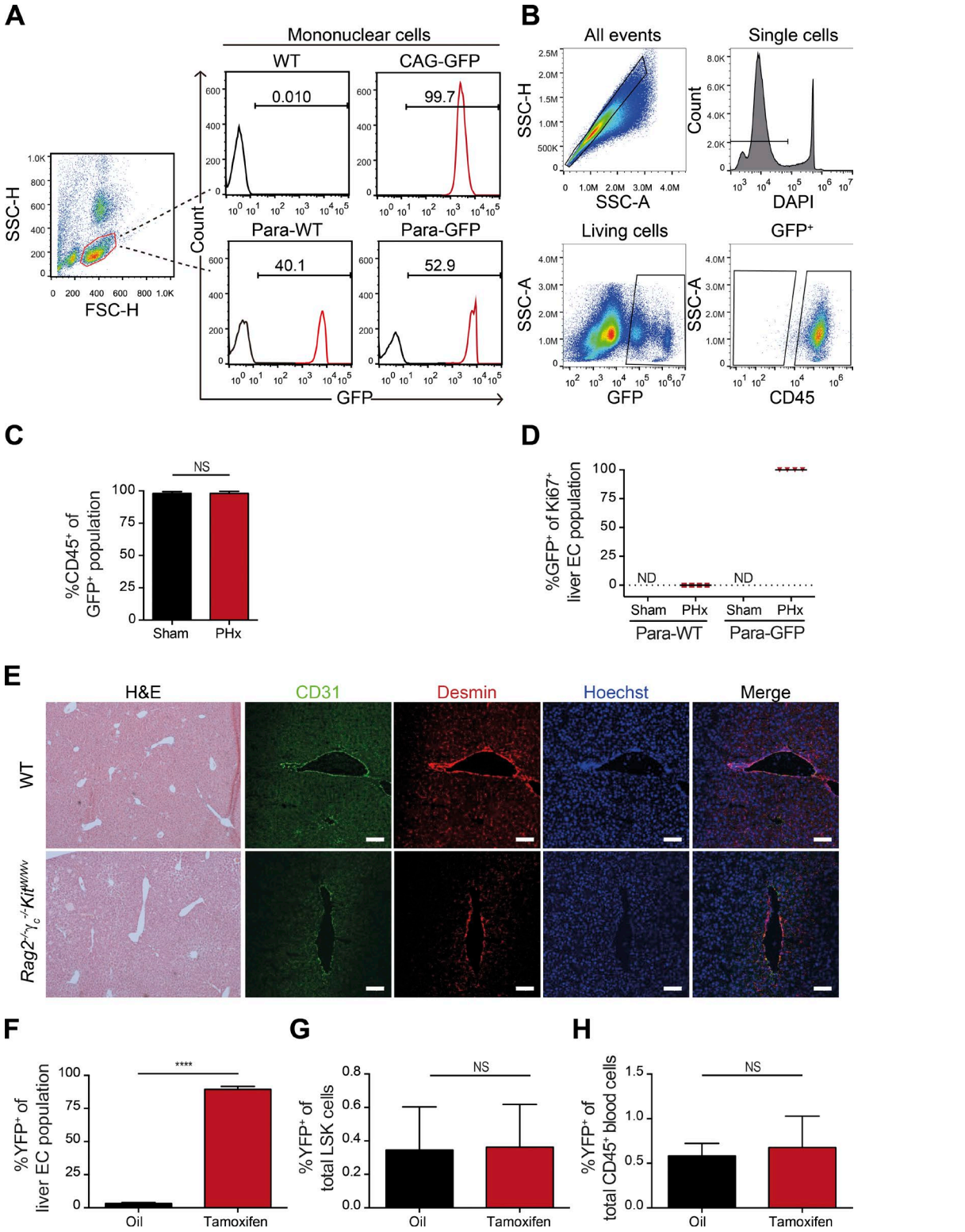

Figure S2. **Nonmyeloablative mouse models to study liver regeneration. (A)** FACS analysis of blood chimerism of parabiosed WT (Para-WT) and GFP (Para-GFP) mice. Blood samples from nonoperated WT and CAG-GFP mice served as negative and positive controls, respectively. **(B)** Gating strategy for the analysis of the cell identity of GFP⁺ cells in the livers of Para-WT mice. **(C)** The plot shows the frequency of CD45 positivity among GFP⁺ cells in the liver of Para-WT mice (mean ± SD, *n* = 3–4 mice). **(D)** The plot shows the ratio of GFP⁺ cells among Ki67⁺ liver ECs in Para-WT and Para-GFP mice (mean ± SD, *n* = 3–4 mice). **(E)** PHx was performed on both WT and *Rag2*$^{-/-}\gamma_c^{-/-}$*Kit*$^{W/Wv}$ mice. Immunohistochemistry and immunofluorescence analysis of the livers of WT and *Rag2*$^{-/-}\gamma_c^{-/-}$*Kit*$^{W/Wv}$ mice after PHx indicate normal liver regeneration in *Rag2*$^{-/-}\gamma_c^{-/-}$*Kit*$^{W/Wv}$ mice. Scale bars, 100 µm. **(F–H)** *VECad-Cre*^{ERT2}*xRosa26-YFP*$^{fl/fl}$ mice were transiently administered with either oil or tamoxifen. After a resting period of 1 mo, the frequencies of YFP⁺ cells among liver ECs (F), LSK cells in the bone marrow (G), and circulating immune cells in the peripheral blood (H) were analyzed by FACS (mean ± SD, *n* = 4 mice). ND, nondetectable; ****, P < 0.0001 (two-tailed Student's *t* test).

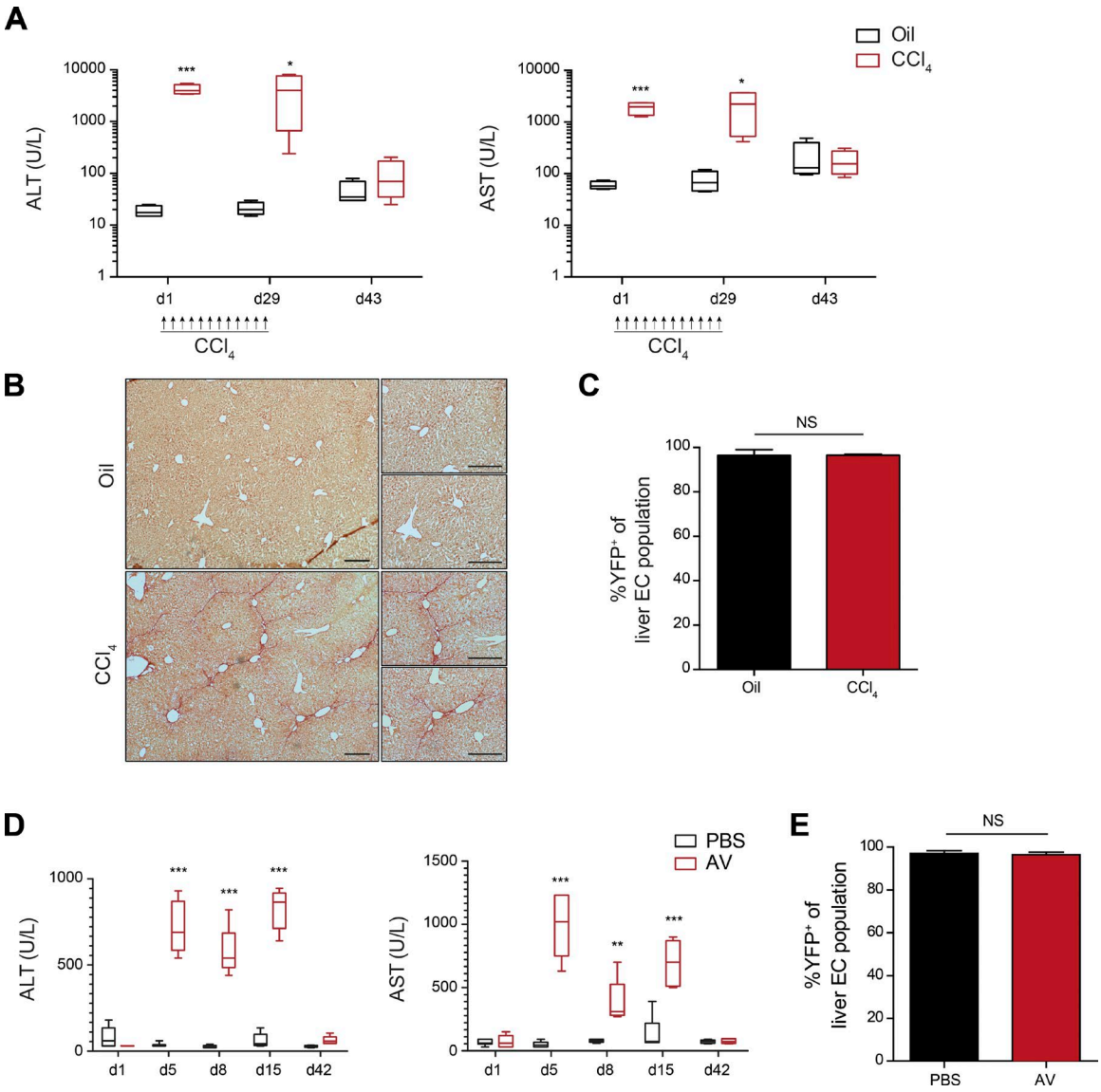

Figure S3. **Liver neovascularization during chronic liver injury. (A–C)** *VECad-Cre^{ERT2}xRosa26-YFP$^{fl/fl}$* mice with labeled liver ECs were repeatedly administered with CCl_4 over a period of 4 wk. **(A)** The plot shows blood plasma ALT/AST levels over the course of the experiment. **(B)** Sirius red staining was performed on the livers of mice treated with either oil alone or with CCl_4. Scale bars, 200 µm. **(C)** The frequency of YFP$^+$ ECs in the livers of *VECad-Cre^{ERT2}xRosa26-YFP$^{fl/fl}$* mice was analyzed by FACS (mean ± SD, n = 4 mice). **(D and E)** *VECad-Cre^{ERT2}xRosa26-YFP$^{fl/fl}$* mice with labeled liver ECs were intravenously injected with 10^{11} viral particles of empty replication–deficient adenovirus. **(D)** The plot shows blood plasma ALT/AST levels over the course of the experiment (mean ± SD, n = 6 mice). **(E)** The frequency of YFP$^+$ ECs in the livers of *VECad-Cre^{ERT2}xRosa26-YFP$^{fl/fl}$* mice was analyzed by FACS (mean ± SD, n = 6 mice). *, P < 0.05; **, P < 0.01; ***, P < 0.001 (two-tailed Student's t test).

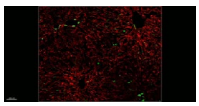

Video 1. **High-resolution three-dimensional reconstruction of liver vasculature demonstrating bona fide integration of fluorescent-labeled elongated EC into the endothelial layer.** ECs in the video are represented in gray; GFP$^+$ cells in green. Surface rendering transparency was set at 50% and recorded at 30 frames per second.